Hindawi
Journal of Engineering
Volume 2023, Article ID 2096501, 18 pages
https://doi.org/10.1155/2023/2096501

Research Article

Performance and Reliability Analysis of Double Boost Converter Fed Renewable PV System

V. Lakshmi Devi,[1] **K. Kumar**,[1] **R. Karpaga Priya**,[2] **and Mohd Asif Shah**[3]

[1]*Department of EEE, Sri Venkateswara College of Engineering, Tirupati 517507, India*
[2]*Department of EEE, Saveetha Engineering College, Chennai, TN 602105, India*
[3]*Kebri Dehar University, Kebri Dehar, Somali 001, Ethiopia*

Correspondence should be addressed to Mohd Asif Shah; drmohdasifshah@kdu.edu.et

Received 5 December 2022; Revised 20 December 2022; Accepted 18 March 2023; Published 30 March 2023

Academic Editor: Prince D. Winston

The article gives the performance and reliability analysis of renewable PV systems fed with a double boost converter. For analyzing the PV system performance and reliability, a 660 W PV system is considered and a double boost converter with the PSO MPPT method is implemented by adding a secondary path to the conventional boost converter, which shares the input current and reduces the current ripples in the system. For a detailed analysis of the system, different solar irradiations of 1000 W/m^2, variable irradiations, and real-time solar irradiation in the area of $13^0 39^1 29.3^{11}$N $79^0 29^1 09.3^{11}$E on May 2022 are considered and reliability indices are presented at PV system and power electronic converter components. A MATLAB/Simulink environment is chosen for analysis of the proposed system in different conditions.

1. Introduction

The total world energy demand is met by both nonrenewable and renewable energy sources (RES) in fast few decades, but due to the awareness and need for environmental protection, the power generation from nonrenewable energy sources (N-RES) are gradually shifted to renewable energy sources [1–4].

The common and well-known drawbacks of RES are unpredictable and continuously changing concerning variations in climatic conditions. Among all the RES, photovoltaic (PV) sources attain a major role in meeting the load demand [5–7]. The total grid-tied system installed capacity reaches 502.7 MW as of 31st August 2022, which includes off-grid applications of 830373 kW of street lighting, 1723479 kW of home lighting, 7948219 kW of solar lanterns, 86830 kW of solar pumps, and 216407.67 kW of standalone power plants. The overall contribution of PV sources is 51% of the total available resources [8].

Renewable energy source researchers mainly focus on extracting the maximum amount of power when it is available and stepping up/down to meet the load demands. To achieve these two targets, power electronic converters (PEC) play a key role in the operation and control of the renewable system.

The low voltage of the PV panel is stepped up for load application with the help of a DC-DC converter. A high gain converter is thus required for a PV system. A nonisolated converter can be used, but they must be efficient when carrying high currents from low voltage sources [9–11].

For applications like low-voltage renewable power sources, typical DC-DC converter duty cycles need to be extended. When getting a high voltage gain of nine or more, the duty cycle plays a key role, and it becomes difficult to maintain high efficiency. It causes voltage strains and requires high-blocking-voltage switches, causing extra losses [12–15].

Low input voltage increases switch current. The full-duty cycle causes diode reverse recovery troubles due to high-amplitude current spikes in output capacitors and diodes. Switching and conduction losses increase [16–18]. The renewable energy system is required a high gain DC-DC

converter with less switch/converter component count, an intelligent MPPT controller, an advanced battery management system, reliability and selection of power components, and system design. A detailed review of the above topics is presented as follows.

Serially discharging parallel-charging capacitors boost converter gain, multiple recharges boost voltage, adds system components, without magnetic components, and this technology allows a hybrid integrated circuit (HIC) converter. A switched capacitors converter and boost converter [19–21] give high voltage gain, adequate duty cycle, high efficiency, and adjustable output voltage. References [22, 23] suggest a switchable-capacitor converter. This article discusses how resonance influences voltage gain.

The authors of reference [24, 25] discuss coupled-inductor converters. An inductor converter can gain voltage without a 100% duty cycle. A leaky inductor can produce voltage overshoots across the switches, which increases switching losses and reduces converter efficiency. A voltage clamp can be used to reduce switching power losses when using lower-rated transistors. References [26, 27] show boost converters with up to 20-volt gain and 97% efficiency. A linked inductor and series-switched capacitor maximize converter voltage gain. The clamp circuit restores power lost to leakage inductance, ensuring efficiency. There are now numerous different converter topologies that have been discovered, making it difficult to determine which one provides the best performance. The complexity of the converter should be considered throughout the selection process. You need to calculate the size, weight, power, and projected efficiency.

In this article, a 660 W PV system with a double boost converter with particle swarm optimization approach is built and implemented by adding the secondary path to the standard boost converter, which shares the input current and decreases current ripples in the system. Different sun irradiations of 1000 W/m^2, variable irradiations and real-time solar irradiation in the area of $13^0 39^1 29.3^{11}$N $79^0 29^1 09.3^{11}$E on May 2022 are evaluated and analyzed for system performance evaluation.

Another important issue in the renewable PV system is its reliability and sensitivity as it is highly fluctuating and unpredictable in nature. Hence, the reliability and sensitivity analysis of a double-boost (DB) converter fed PV system is presented in this paper. Reliability and sensitivity prediction in power electronic converters become the most important challenge to the converter manufacturers during the burn-in and wear-out period and to the converter user/researcher during the life period. If the converter failure occurs in the useful life period, the entire system power flow will get affected. Manufacturers will take care of the burn-in period, if a failure occurs also, it will not affect more to the system, more since it is in the infant stage.

The reliability and sensitivity of PEC are tested in the burn-in period by the manufacturers, but after it came to the useful lifetime period, where actual converter operation starts, specific care to be taken to avoid converter failure, if the failure occurs, it stops the entire power flow operation, and with this the system is nonreliable to meet the load demand. Detailed reliability indices are presented for the design of renewable PV systems in the following chapter.

The following is the outline of the study: we will go over the simulations of the proposed PV installation. The modeling of the DB Converter and the parameters employed in the planned design is discussed in detail in the third section. The Multiphase Power Flow Controller is explained here. Succeeding Section displays the outcomes of incorporating MATLAB/Simulink into the proposed system. Developed system PV system and Power Electronic converter dependability indices are summarized in succeeding Section, and then the conclusion is presented in succeeding Section.

2. Proposed PV System Model

Inputs δ_1 and δ_2 are outputs for creating a double boost output voltage. The DB converter is built with two switches, two inductors, and two diodes, as illustrated in Figure 1.

Table 1 provides the module type, number of series and parallel linked modules per string, V_{OC}, I_{SC}, V_{MP}, I_{MP}, and series and parallel resistance of the Canadian Solar CS5P-220M solar PV module.

Figure 2 illustrates the I-V and P-V characteristics of 218 W PV panels at 0.25 kW/m^2, 0.5 kW/m^2, 0.75 kW/m^2, and 1 kW/m^2. Figure 3 illustrates the I-V and P-V characteristics of a 660 W PV module at 0.25 kW/m^2, 0.5 kW/m^2, 0.75 kW/m^2, and 1 kW/m^2. This 660 W system includes three parallel strings and one series-connected module per string.

The input for the proposed DB converter system is 48.32 V obtained from the PV module and the required load voltage is of 380 V. To increase the voltage from 48.32 V to 380 V, a DB converter is operating at the duty cycle of 0.873. As the input voltage is less, there is a high amount of current ripples at the input side. The developed PV system with DB converter will reduce reduced current ripple by providing parallel paths current flow.

3. DB Converter Analysis

The DB converter splits the input current by cascading a control switch, inductance, and diode. The cascaded boost converter features a 180-degree phase delay; the total input current is the sum of L_1 and L_2 inductor currents, which minimizes input current amplitude and ripples.

Depending on D, each phase's switching sequences may overlap. The ON duration of each switch determines the DB converter's functioning. The DB converter has two purposes when both switches are ON. Duty cycle between 0 and 0.5 in area −1 and 0.5 and 1 in area −2 region 1 has no simultaneity. It is a no-go zone. When only the switch turns off, the inductor cannot be demagnetized. Region 2 has two on-at-once switches and converter design parameters are presented in Table 2.

The output voltage,

$$V_o = \frac{1}{1-D} * V_{PV}. \quad (1)$$

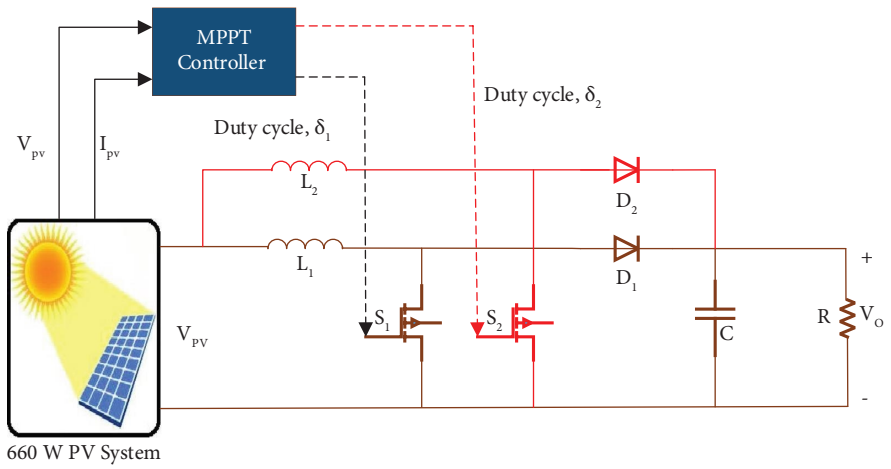

Figure 1: Block diagram of the system.

Table 1: PV system specifications.

Parameters	Specifications @ STC
Module type	Canadian solar CS5P-220M
Current, I_{mp}	4.51758 A
Series resistance, R_s	0.24807 ohm
Voltage, V_{mp}	48.3159 V
Parallel resistance, R_p	235.76 ohm
Parallel strings	3
Short circuit current, I_{sc}	5.09261 A
Series connected modules per string	1
Open circuit voltage, V_{oc}	59.2618 V
Phase current, If	5.098 A
Saturation current, I_{sat}	$5.3103e^{-7}$ A

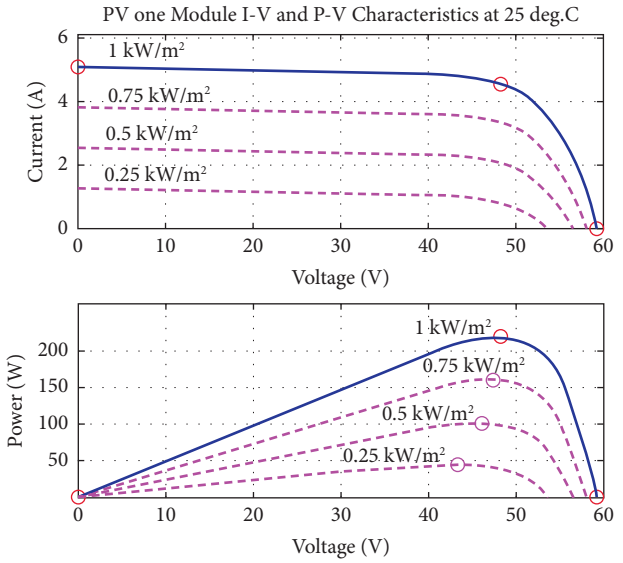

Figure 2: I--V and P-V characteristics of 218 W PV panel.

Input current,

$$I_{PV} = \frac{P_{PV}}{V_{PV}}. \quad (2)$$

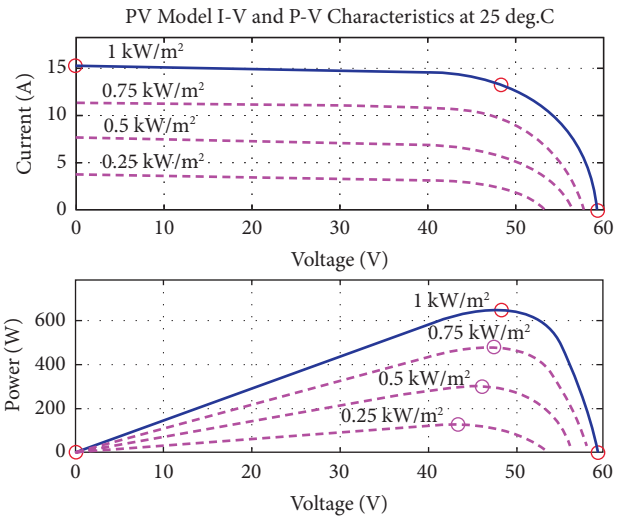

Figure 3: I-V and P-V characteristics of 660 W PV modules.

Table 2: Converter design parameters.

Parameter	Rating
Power	660 W
Voltage (input and output)	48.32 V and 380 V
Inductor (L_1 and L_2)	4.3 mH and 4.75 mH
Capacitor (C_1 and C_2)	17.23 μF and 5.75 μF
Load resistor, R	220 Ω
Switching frequency	20 kHz

Inductor current ripples,

$$\Delta I_{L1} = \frac{V_{PV} * D}{f_s * L_1}, \qquad \Delta I_{L2} = \frac{V_{PV} * D}{f_s * L_2}. \quad (3)$$

Converter components calculations

$$L = \frac{V_{PV} * D}{f_s * \Delta i_L}. \tag{4}$$

By considering the 2% peak-peak capacitor ripples

$$C = \frac{V_{PV} * D}{R * \Delta V_o} = \frac{V_{PV} * D}{R * T_s * C_o}. \tag{5}$$

3.1. Operating Modes of DBC

3.1.1. Mode-1: ($0 < t < t_1$). Switches S_1 and S_2 activate Mode-1 and reverse bias diodes D_1 and D_2. Inductors L_1 and L_2 have linearly growing currents. Capacitor, C powers the load, as shown in Figure 4.

3.1.2. Mode-2: ($t_1 < t < t_2$). This stage begins when S_2 is turned off and D_2 is reverse-biased. Demagnetizing L_2 reduces i_{L2} linearly. Diode D_2 transfers energy between the source and load. Figure 5 shows this topological phase.

3.1.3. Mode-3: ($t_2 < t < t_3$). The third topological stage is the same as the first stage, as shown in Figure 6.

3.1.4. Mode-4: ($t_3 < t < t_4$). Demagnetized L_1 inductor current drops linearly. Diode D_1 transfers power between the source and load. Figure 7 shows this period. After stage 4, the changeover time ends and stage 1 begins.

The theoretical switching waveform for the DB converter is shown in Figure 8. The summary of the proposed DB converter modes of operation with switching states and inductor chagrining and discharging conditions is listed in Table 3.

4. MPPT Algorithm

The DC-DC converter's ideal duty ratio determines the optimal voltage and current combination for maximum power. Many MPPT control strategies [28–30] have strengths and downsides. This paper considers particle swarm optimization (PSO) based MPPT to extract maximum.

PSO mimics bird flocks. Global convergence makes PSO acceptable for nonlinear, nondifferential curves [29]. The intermittent supply makes the MPPT method curve nonlinear. PSO uses n-dimensional cooperative points to find a global optimization solution.

PSO was inspired by flocks of birds. Each particle (x_i) in a swarm represents a possible solution, whose position is changed based on the neighbourhood best particle (P_{besti}) and the global best particle (G_{best}) during each iteration (t). Equation (7) updates particle position x_i.

$$x_i^{t+1} = x_i^t + \Phi_i^{t+1}; \quad i = 1, 2, \cdots\cdots \tag{6}$$

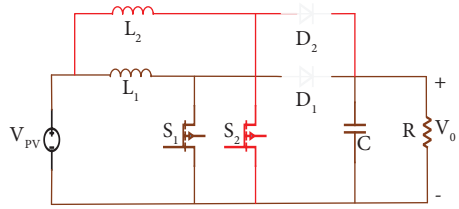

Figure 4: Mode-1: S1-ON, S2-ON.

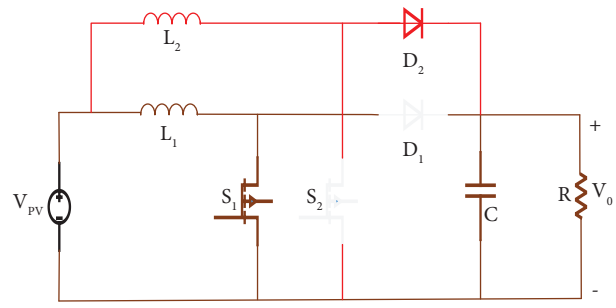

Figure 5: Mode-2: S1-ON, S2-OFF.

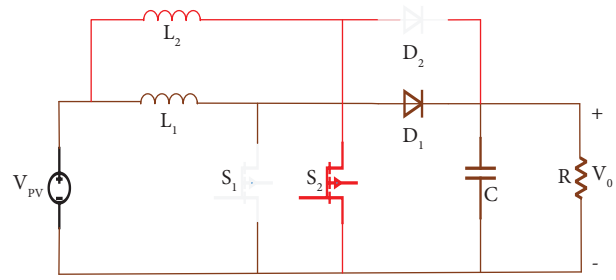

Figure 6: Mode-3: S1-OFF, S2-ON.

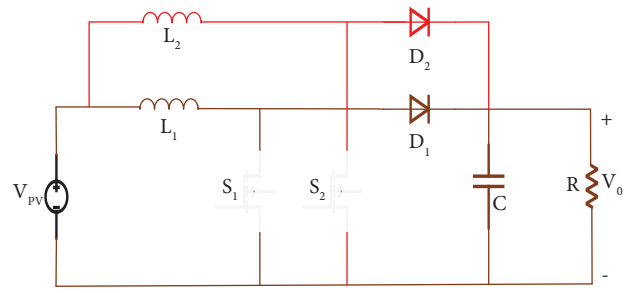

Figure 7: Mode-4: S1-OFF and S2-OFF.

where the velocity gradient ø reflects the stochastic step and is calculated as follows:

$$\Phi_i^{t+1} = w * \Phi_i^t + r_1 c_1 \left(P_{\text{besti}} - x_i^t\right) + r_2 c_2 \left(G_{\text{best}} - x_i^t\right). \tag{7}$$

In equation (8), the second and third terms represent the cognitive and interpersonal contributions, with their corresponding constants c_1 and c_2, correspondingly. The first term w represents the inertial weight. r_1 and r_2 are examples of random numbers inside the range of (0-1).

The fundamental operating principle of this approach:

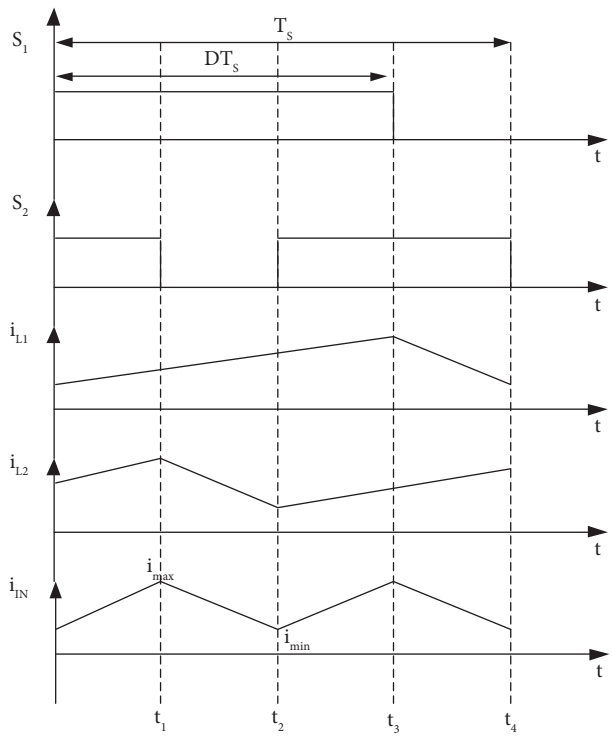

Figure 8: DB converter switching waveform.

Step 1. (Initialization):

Particles are frequently initialized randomly over the search space using a uniform distribution or on-grid nodes that fill the search space with equidistant points. Initial velocities are chosen at random.

Step 2. (Fitness evaluation):

Determine the fitness of each particle. The fitness of the candidate is assessed by supplying a solution to the objective function.

Step 3. (Updating individual and global best data):

By comparing newly calculated optimal solution to old ones and updating the P_{besti} and G_{best} as necessary, we maintain accurate rankings of the individuals with the highest and best fitness levels.

Step 4. (Updating velocity and position of each particle):

Steps 1 and 2 are used to perform updates on the velocity and position of each particle in the swarm (2).

Step 5. (Determining convergence):

If the convergence criterion is met, the procedure can be finished; otherwise, the number of iterations increases by one and the process returns to Step 2.

Figure 9 shows that the gate pulse for Converter-1 and Converter-2 and the converter operates in two power stages with 180 degrees out of phase and it provides a two-to-one reduction in peak-to-peak ripple current. To generate the gate pulses, PSO-based MPPT techniques are used for the extraction of the maximum possible power in the PV system.

5. Simulation Results and Discussion

The MATLAB/Simulink model of the proposed 660 W PV system is shown in Figure 10. The system uses a DB converter and an MPPT method based on particle swarm optimization. Pulses for the DB converter are generated by the PSO MPPT algorithm based on the measured V_{PV} and I_{PV}, allowing for maximum power extraction from the available solar irradiance and input meteorological conditions.

The overall PV system performance is investigated in three situations based on solar input irradiations and temperature. In Case 1, continuous solar irradiation of 1000 W/m^2, variable irradiance ranging from 600 W/m^2 to 1000 W/m^2 over different periods, and real-time solar irradiation data on May 2022 over one day are examined in MATLAB/Simulink, and PSO MPPT is used to analyze the proposed system's performance.

Case 1. Constant solar irradiation.

Figure 11 shows the constant solar irradiation data of 1000 W/m^2 and a constant temperature of 25°C as input to the 660 W PV system. The proposed system consists of two inductors L_1 and L_2 for providing parallel paths for current sharing.

Figure 12 shows the input current at inductor L_1 of 7 A and L_2 of 7 A of Converter-1 and Converter-2, respectively. The double boost converter will operate with a phase delay of 180° as clearly presented with currents (L_1 and L_2) in zoom mode.

Figures 13 and 14 show the input voltage (48 V), current (7 A), and power (330 W) at Converter-1 and Converter-2, respectively. Similarly, Figure 15 displays the output voltage (380 V), current (1.5 A), and power (600 W), respectively, at the load side.

From the analysis of the proposed system with constant solar irradiation data in Case 1, the proposed double boost converter will share the input currents through inductors L_1 and L_2 with the help of diodes, and which reduces the current level and current stress on the proposed converter switches.

Case 2. Variable solar irradiation.

Figure 16 shows the considered solar irradiation data in Case 2 as follows, for a period of 0 to 0.4-sec available solar irradiation is 600 W/m^2, similarly, for a period of 0.4 to 0.8, 0.8 to 1.2, 1.2 to 1.6, 1.6 to 2, and 2 to 2.4-sec available solar irradiation is 750 W/m^2, 900 W/m^2, 1000 W/m^2, 800 W/m^2, and 700 W/m^2, respectively.

Based on the considered solar irradiation data in Case 2, Figure 17 shows the input inductor currents (L_1 and L_2) of Converter-1 and Converter-2, respectively. The double boost converter will operate with a phase delay of 180^0 as clearly presented with currents (L_1 and L_2) in zoom mode.

Figures 18 and 19 present the input voltage at Converter-1 and Converter-2, respectively, as per the considered solar irradiation in Case 2. Similarly, Figure 20 shows the output voltage, current, and power at load, respectively, at the load side.

Table 3: DB converter modes of operation.

Mode	Converter-1 switch, S_1	Converter-2 switch, S_2	Inductor, L_1	Inductor, L_2
Mode-1	ON	ON	Charging	Charging
Mode-2	ON	OFF	Charging	Discharging
Mode-3	OFF	ON	Discharging	Charging
Mode-4	OFF	OFF	Discharging	Discharging

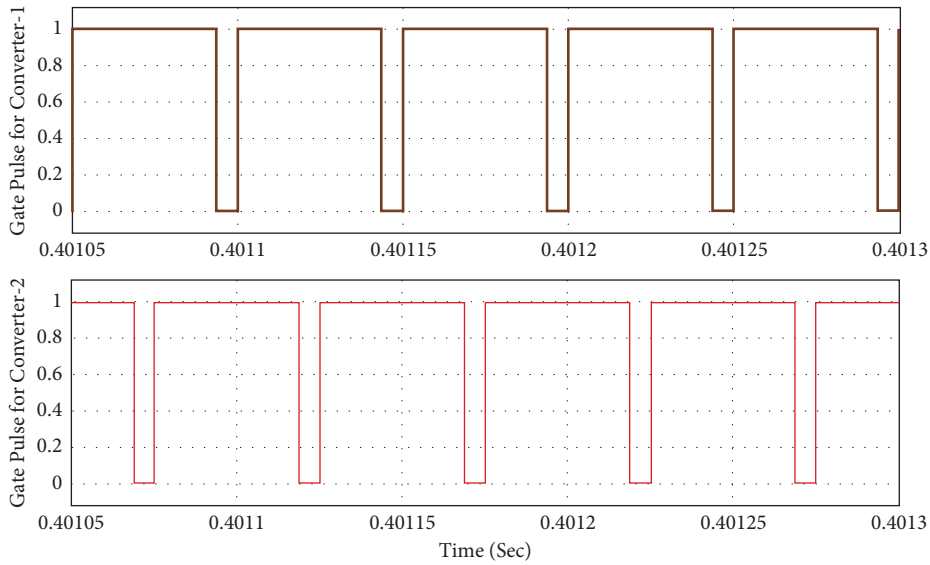

Figure 9: Pulse generation.

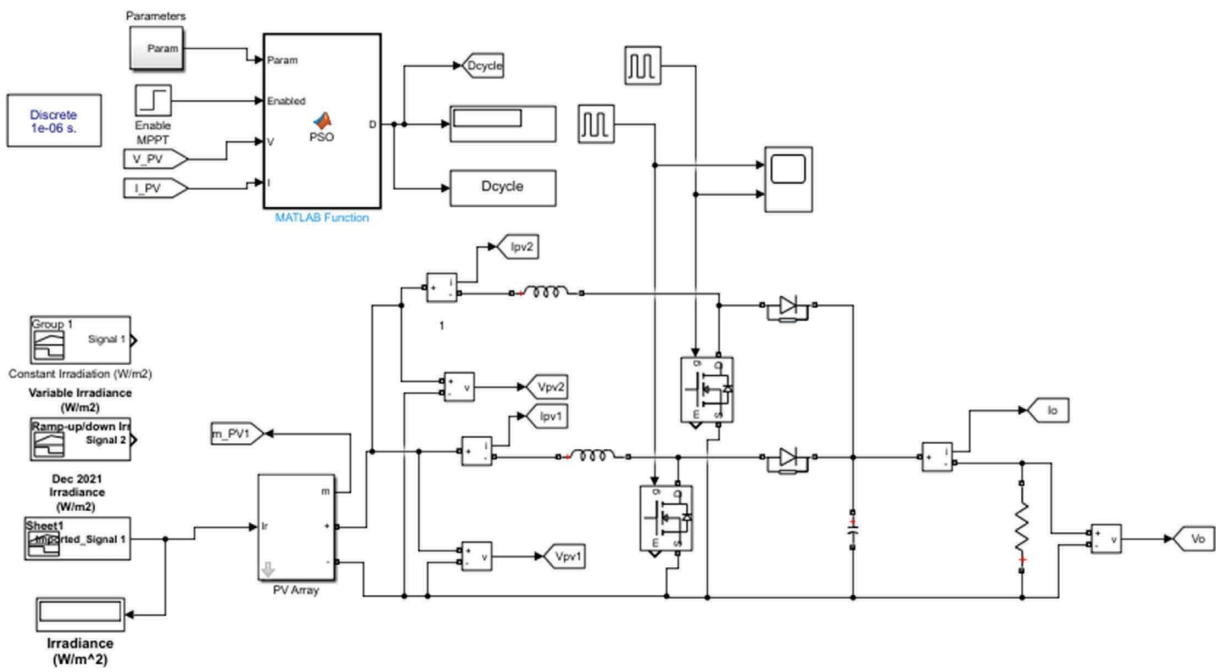

Figure 10: Simulink model of the system.

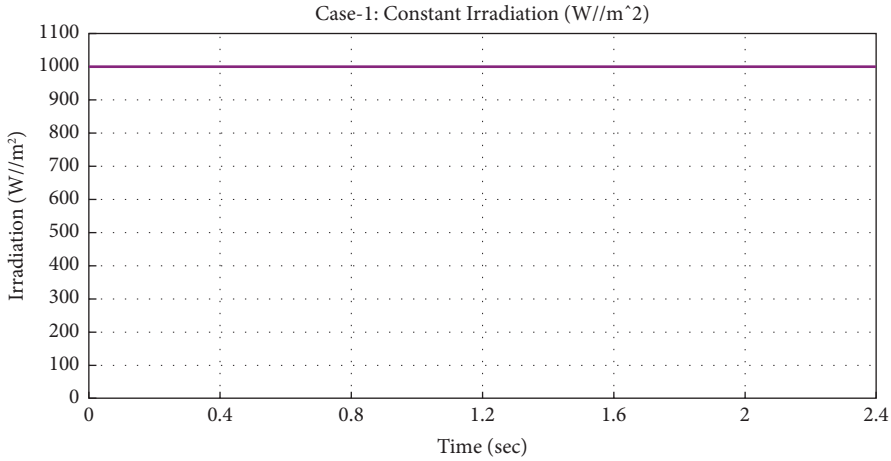

Figure 11: Input solar irradiation in Case 1.

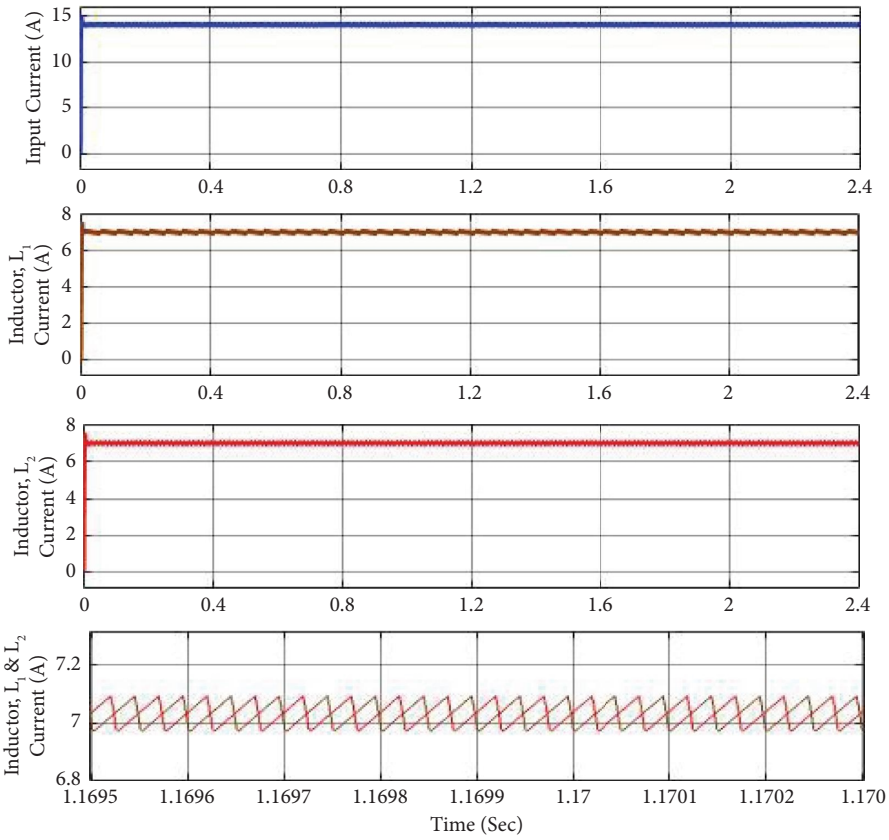

Figure 12: Current profile at input, inductor L_1, inductor L_2, and combined L_1 and L_2.

From the analysis of the proposed system with constant solar irradiation data in Case 2, the proposed double boost converter will share the input currents through inductors L_1 and L_2 with the help of diodes, which reduces the current level and current stress on the proposed converter switches.

Case 3. Real-time data of solar irradiation data on May 2022.

The performance of the proposed system with real-time solar irradiation data was considered in the region of $13^0 39^1 29.3^{11}$N $79^0 29^1 09.3^{11}$E in May 2022. Figure 21 shows the considered real-time solar irradiation data in Case 3.

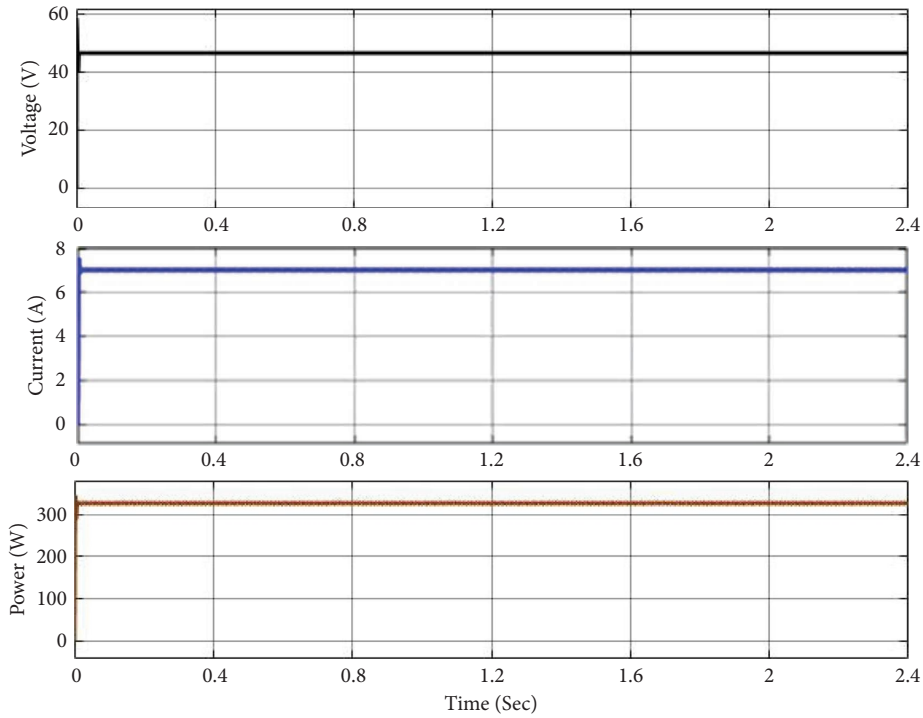

Figure 13: Input voltage, current, and power at converter-1.

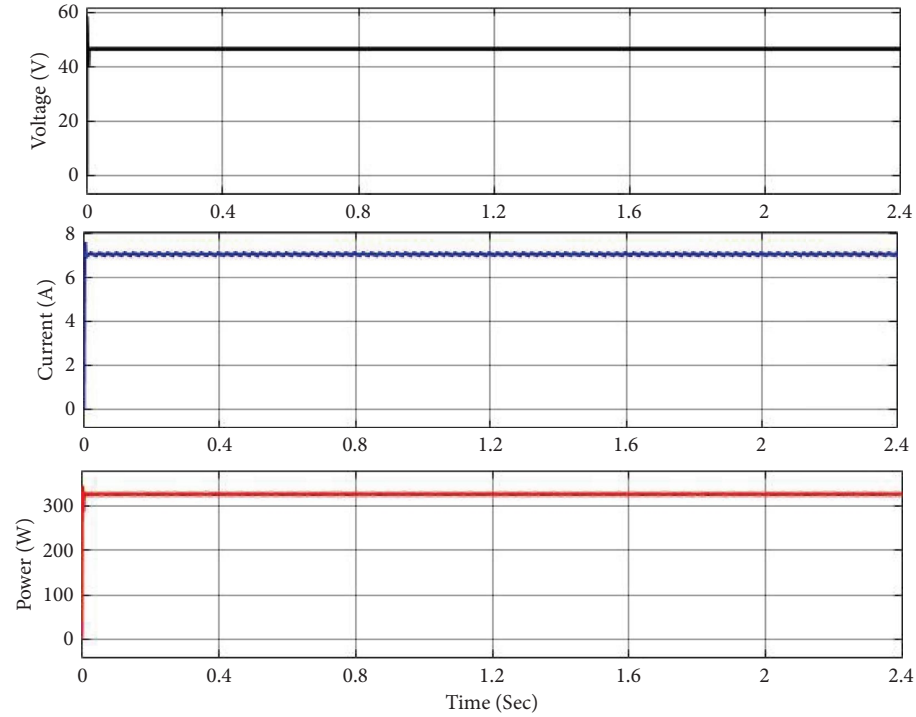

Figure 14: Input voltage, current, and power at converter-2.

Based on the considered solar irradiation data in Case 3, Figure 22 shows the input inductor currents (L_1 and L_2) of Converter-1 and Converter-2, respectively. The double boost converter will operate with a phase delay of 180^0 as clearly presented with currents (L_1 and L_2) in zoom mode.

Figures 23 and 24 illustrate the input voltage at Converter-1 and Converter-2 for Case 2. Figure 25 shows the load side voltage, current, and power. Based on the examination of the proposed system with constant solar irradiation data in Case 3, the proposed double boost converter

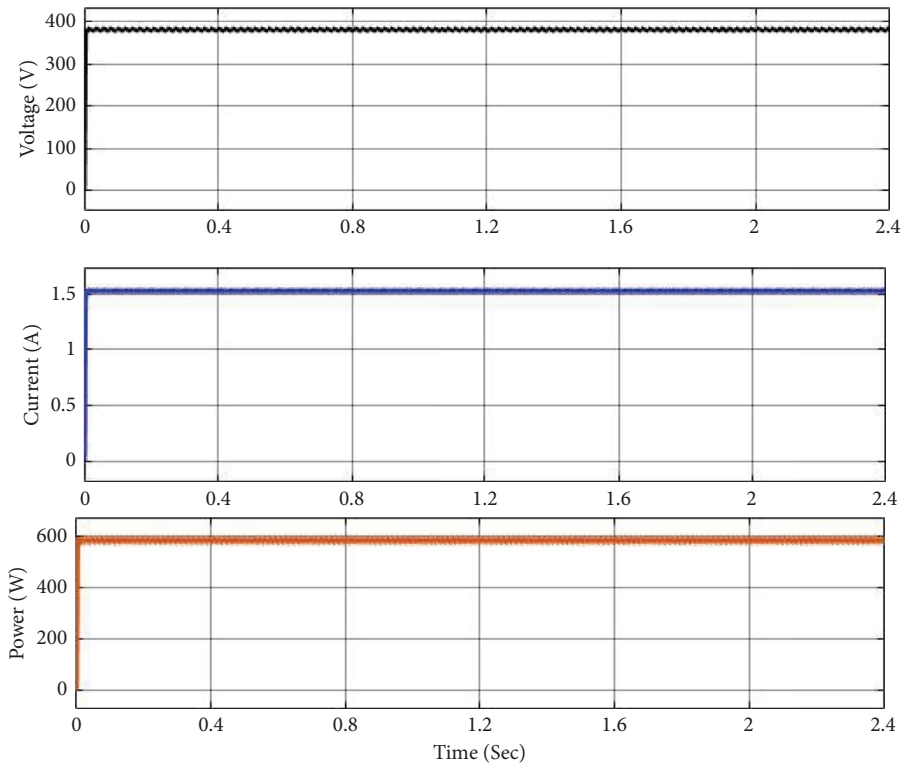

Figure 15: Output voltage, current, and power at load.

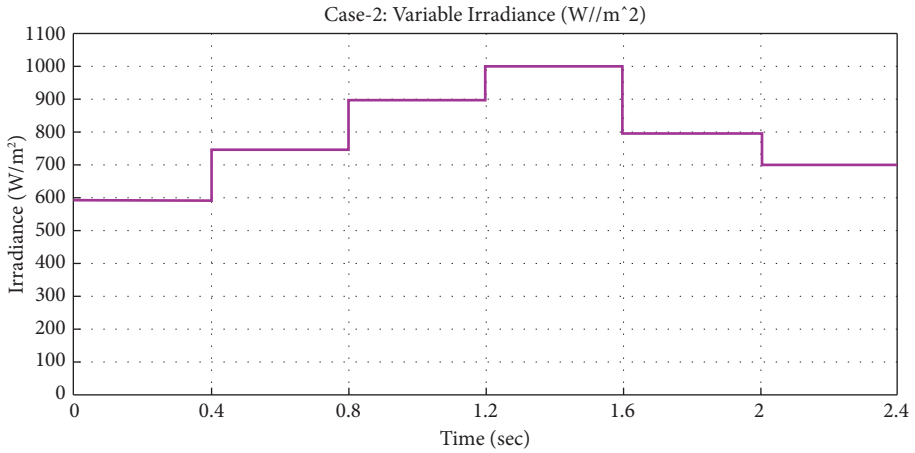

Figure 16: Input solar irradiation in Case 2.

will share the input currents through inductors L_1 and L_2 with the help of diodes, reducing the current level and the current stress on the proposed converter switches.

6. Reliability Exploration of the Proposed System

Reliability analysis of power electronic components is important for the PE component manufacturers to provide the complete information in the datasheet of PE components to create the awareness of reliability and costs of the PEC throughout the life span [30–32].

It provides complete information about system design and reliability of the system from component level to overall system, which helps in selecting optimal choices for system upgradations and modifications.

Reliability deals with finding the ability of the system to work without failure over a time period under given conditions. In general, the system's dependability, as well as economic and environmental indices are taken into account [33–35].

6.1. Reliability and Sensitivity Analysis of the PV System. Solar PV system sensitivity and reliability are affected by variable solar irradiation and operating temperature. The literature provides PE converter sensitivity and reliability indexes. This case study uses Markov model reliability

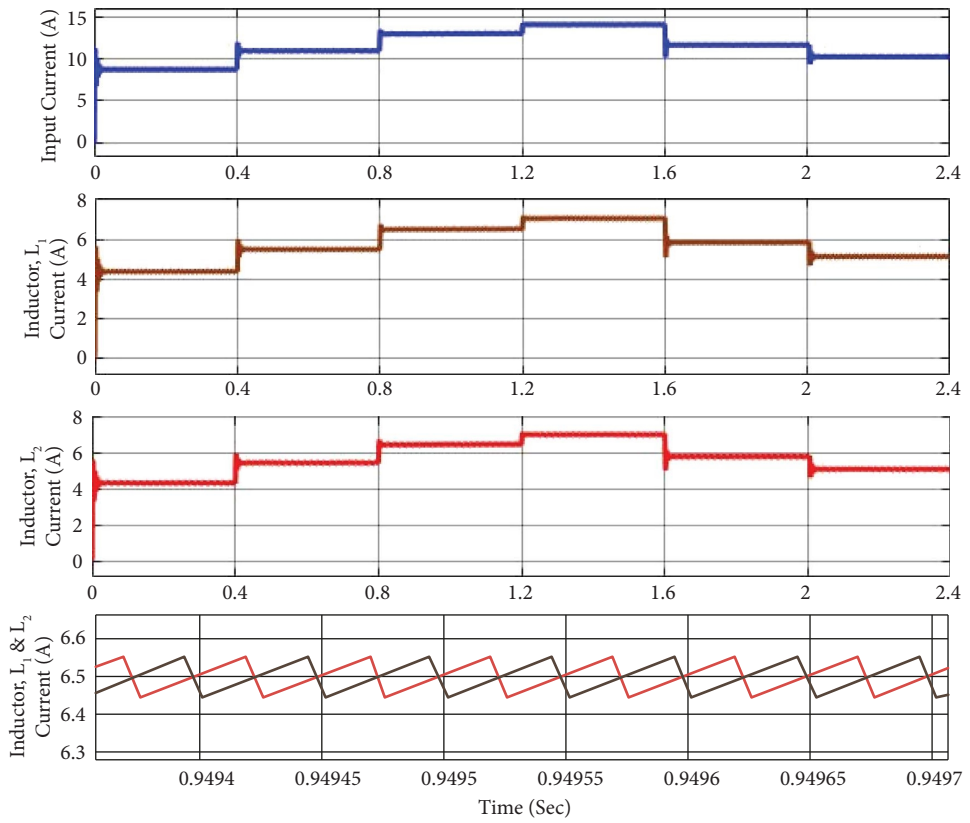

Figure 17: Current profile at input, inductor L_1, inductor L_2, and combined L_1 and L_2.

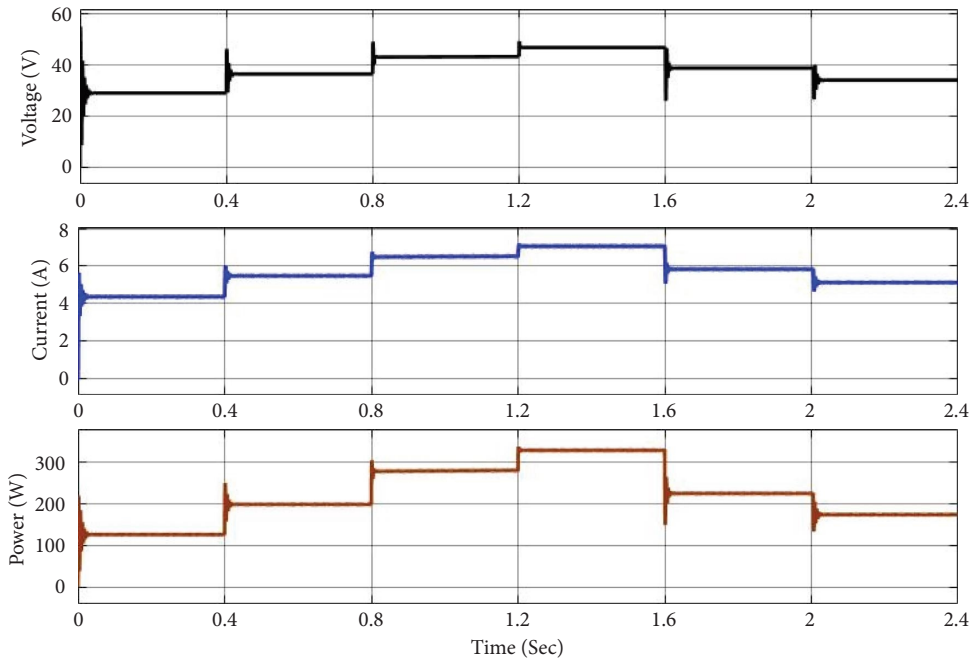

Figure 18: Input voltage, current, and power at Converter-1.

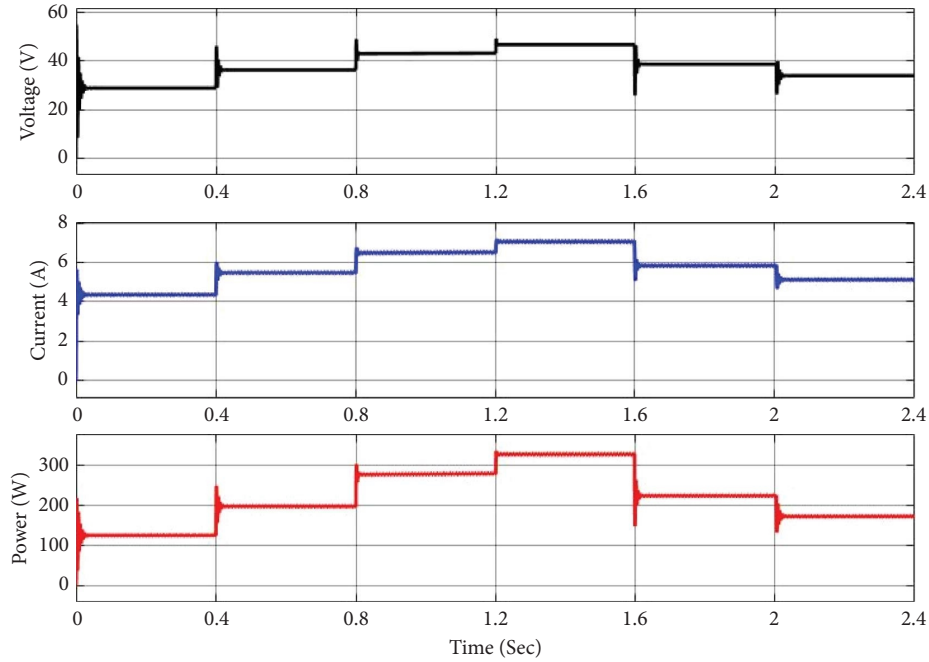

Figure 19: Input voltage, current, and power at Converter-2.

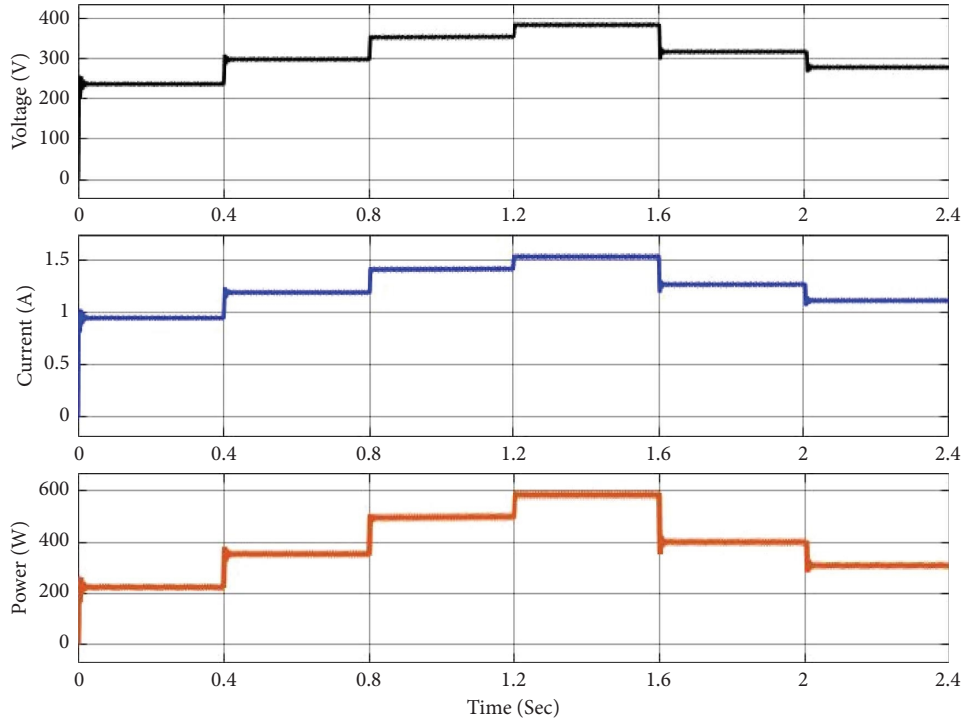

Figure 20: Output voltage, current, and power at load.

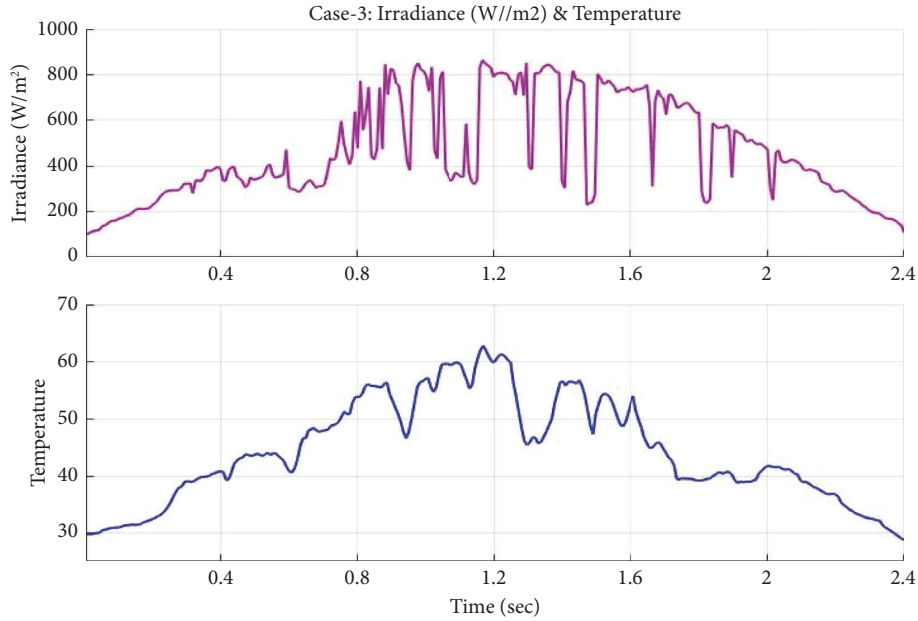

Figure 21: Real-time solar irradiation and temperature data.

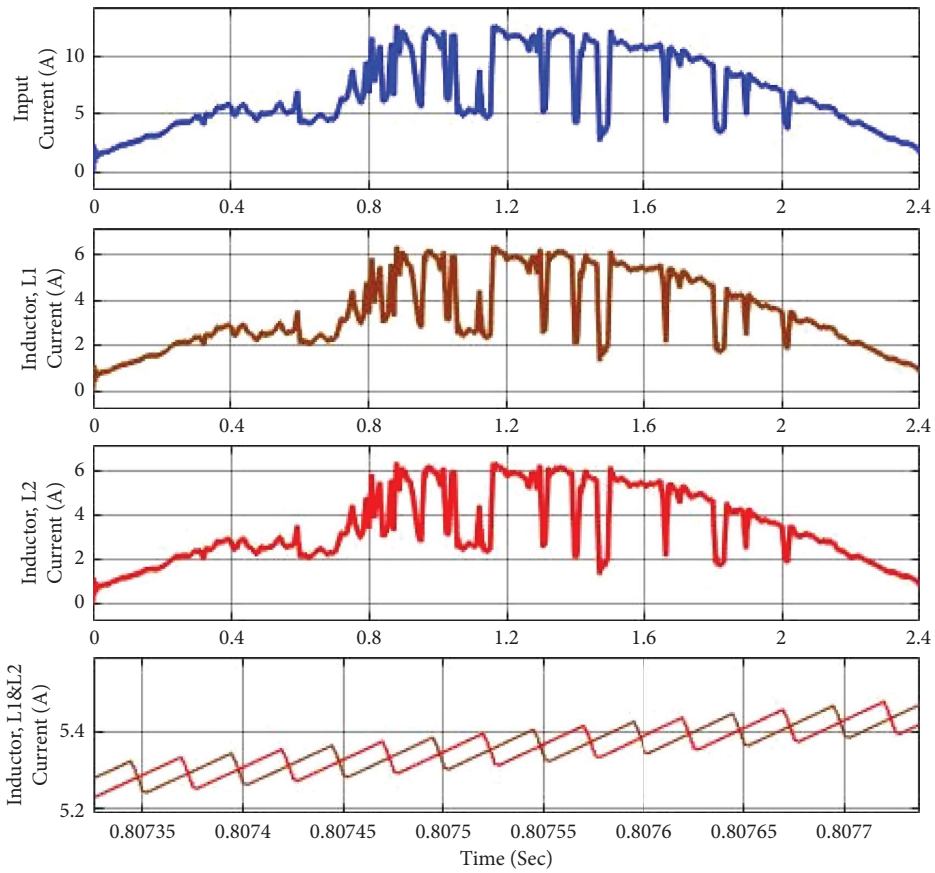

Figure 22: Current profile at input, inductor L_1, inductor L_2, and combined L_1 and L_2.

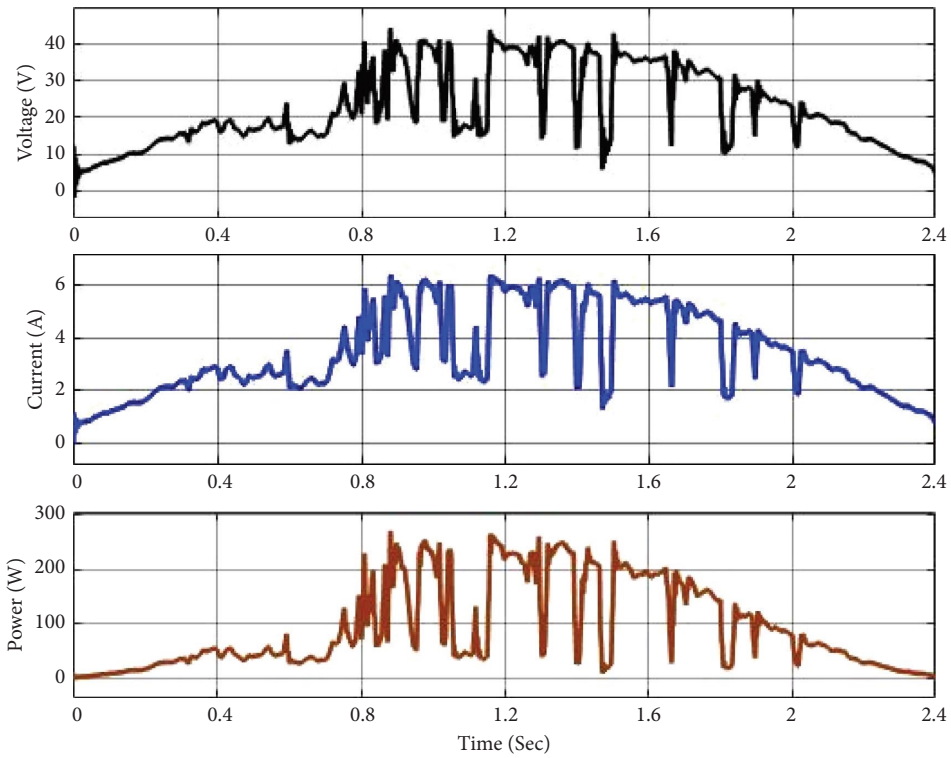

Figure 23: Input voltage, current, and power at Converter-1.

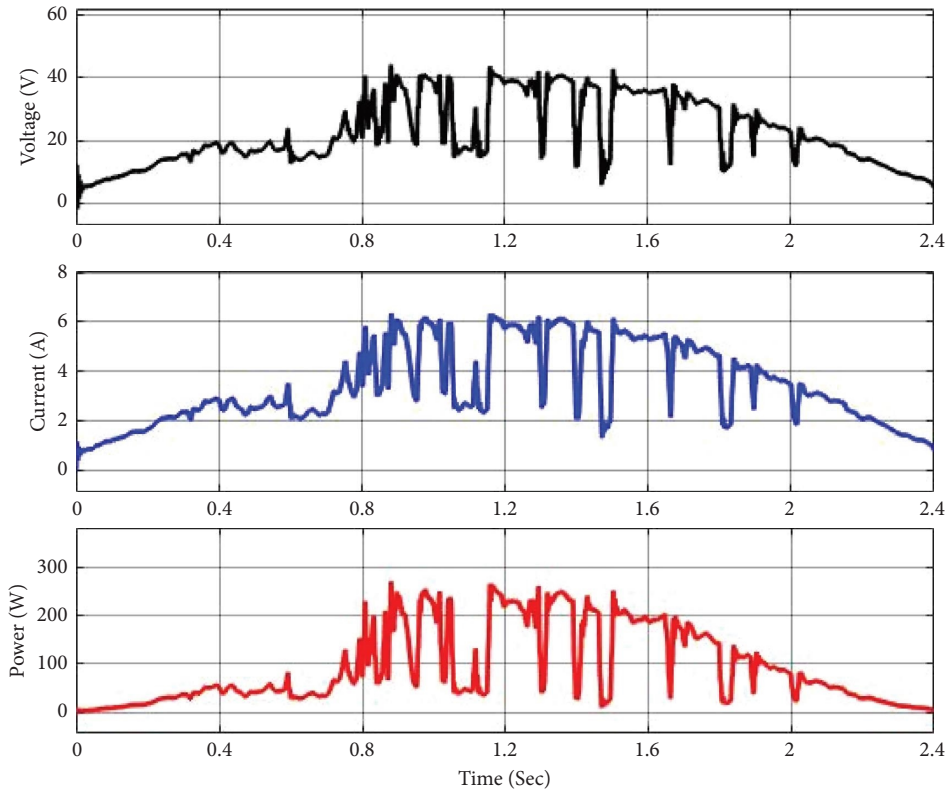

Figure 24: Input voltage, current, and power at Converter-2.

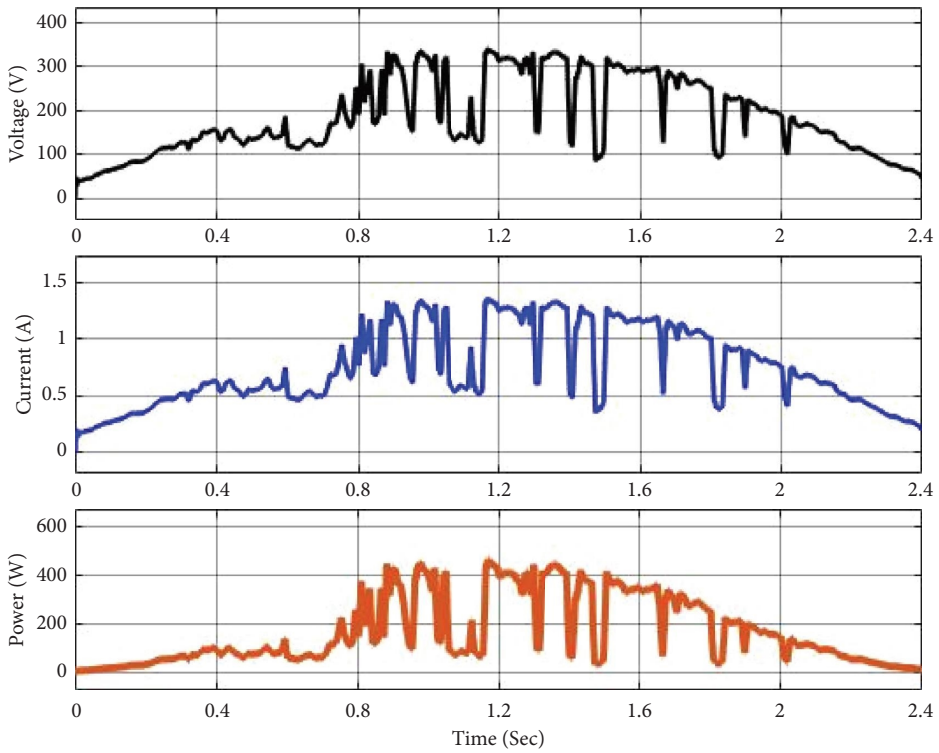

Figure 25: Output voltage, current, and power at load.

indicators. Markov method can be utilized for repairable, nonrepairable, series, parallel, and combination systems. Consider an n-component series system.

Figure 26 depicts n system components. Proper system operation depends on all system components. Using the Markov model, steady state availability (A) and unavailability expression U are given in equations (8) and (9).

$$A = \frac{\mu}{\lambda + \mu}, \tag{8}$$

$$U = \frac{\lambda}{\lambda + \mu}. \tag{9}$$

Since for any practical system, the unavailability expression is written as in equation (10)

$$U = \lambda * r, \tag{10}$$

where $r = 9760/\mu$hrs, μ occurs/year

Table 4 gives the failure rate and repair times of the PV system for the reliability analysis of the renewable PV system.

6.2. Power Converter Component's Reliability Indexes. Common criteria for evaluating power electronic systems include dependability, failure rate, MTTF, MTTR, and availability.

6.2.1. Reliability. The possibility that an object (component, subsystem, or system) will perform required functions for the planned time is defined as reliability. The reliability function $R(t)$ measures the probability of system failure throughout the range $[0, t]$.

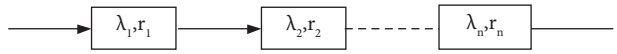

Figure 26: Series connected system.

Figure 27 displays the reliability "bathtub curve," which predicts the cradle-to-grave instantaneous failure rate vs. time for specific devices. Exponentially modeled curve system reliability is time-dependent. Time decreases reliability. Time should cover commercial product warranties.

6.2.2. Failure Rate. The failure rate of the product after t years can be used to evaluate a product's "propensity to fail" Figure 27 depicts a bathtub curve, which is a failure rate curve shown as a function of time. According to the bathtub curve seen in Figure 27, an object's lifespan can be divided into three separate stages: burn-in, useable life, and wear-out. Despite the extensive testing, there was a substantial failure rate during the burn-in period due to design or manufacturing flaws that were not discovered. If a product survives the early "burn-in" stage, its failure rate will grow more constantly over a period of time before it fails. Systems fulfilled their tasks while they were worn out. As a result, the rate of failure over the useful lifetime of a product is an important aspect of dependability analysis. As shown in equation (11), the failure rate $\lambda(t)$ is related to the reliability function $R(t)$.

Table 4: Failure rate and repair times.

S. No	Modules	Failure rate/yrs	Repair time (hrs)	Repair time (yrs)
1	PV array	0.045	35	250
2	DC-DC converter	0.04	40	219
3	Inverter	0.095	40	219
4	Switch	0.075	30	292

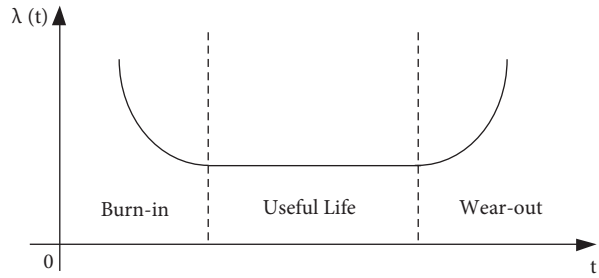

Figure 27: Failure rate curve.

$$\lambda(t) = \lim_{\Delta t \longrightarrow 0} \frac{R(t) - R(t + \Delta t)}{R(t)\Delta t} = -\frac{1}{R(t)} \frac{dR(t)}{dt}, \tag{11}$$

where Δt is a time interval with $\Delta t > 0$. The reliability $R(t)$ is determined from the failure rate $\lambda(t)$ with the consideration of $R(0) = 1$, as presented in equation (13).

$$R(t) = e^{-\int_0^t \lambda(\tau) d\tau}. \tag{12}$$

It is common practice in the reliability modeling field to assume that the failure rates of components and subsystems are unaffected by the passage of time. However, this assumption is not without its drawbacks. With the assumption that $\lambda(t) = \lambda$, the equation (13) can be reduced as follows: (13)

$$R(t) = e^{-\lambda t}. \tag{13}$$

The success rate is then calculated by taking the mean of the number of failures that occurred in a certain amount of time, which is denoted by the unit failures in time (FIT).

1 FIT $= 10^{-9}$ failure/hour.

6.2.3. Mean Time to Failure (MTTF). The "expected failure time" is denoted by the "MTTF." MTTF is time-independent, unlike dependability. It determines how long something can be used before it succumbs to wear and tear. The MTTF metric is utilized in the process of architecture comparison. This exemplifies how long a product will remain in use. Even though the MTTF is significantly longer than the mission time, this does not necessarily guarantee that the system is particularly dependable when it is being used on the mission.

Equation (14) provides an explanation of MTTF and dependability.

$$\text{MTTF} = \int_0^{+\infty} R(t) \mathrm{d}t, \tag{14}$$

where $R(t)$ is the reliability function. When the failure rate $\lambda(t)$ is constant λ, and is simplified in equation (15)

$$\text{MTTF} = \frac{1}{\lambda}. \tag{15}$$

6.2.4. Mean Time to Repair (MTTR). Mean time to repair is the amount of time, on average, needed to fix a system once it has failed. The amount of time needed to repair anything is proportional to its maintainability, which includes things like fault diagnosis and replacement parts.

6.2.5. Availability and Average Availability. The degree to which a system is likely to be functional is referred to as its availability. The uptime that a system enjoys on average over a certain time frame is referred to as its average availability. If a repairable system is fixed every time it fails to "as good as new" standards, the equation will read as follows: gives its average availability in equation (16).

$$A_{\text{average}} = \frac{\text{MTTF}}{\text{MTTF} + \text{MTTR}}. \tag{16}$$

Increasing availability necessitates better MTTF and MTTR. Average availability cannot reflect the frequency of breakdowns or maintenance. It is only used to evaluate repairable systems where availability takes precedence over dependability.

Total time/number of failures $(T/R) = \text{MTBF}$. MTF stands for Mean Time to Failure.

To discriminate, you must first comprehend suspensions. When a destructive test or observation fails to detect a failure, reliability calculations are temporarily halted. Suspensions are not included in MTBF, although they are in MTTF. The MTTF is determined by dividing the total number of service hours by the number of devices. When all components fail through the same cause, MTBF approaches MTTF.

T/N, where T is total time and N is the number of test units, equals MTTF.

7. Load Side Reliability Indexes

Many reliability indicators in the current study that comply with the global utility standard emphasized annual load demand and its impact on generator dependability. The following indices are considered to be a loss: LOLP, LOLE, LOEE, LOEP, and EENS. The values of λp and Up are then

utilized to do an analysis of the system reliability indices for each of the six scenarios.

The average failure rate, p, is calculated as follows: (number of loads multiplied by failure rates) + (number of substations multiplied by failure rates) + (number of feeders multiplied by failure rates) + (number of distributed generators multiplied by failure rates).

The length of time that the power is out or unavailable, Up = (number of loads failure rates ∗ Reliability function) + (number of substations failure rates restoration time ∗ Reliability function) + (number of feeders failure rates ∗ Reliability function) + (number of distributed generators failure rates ∗ Reliability function).

7.1. Economic Indexes. Economic indices that account for launch costs, maintenance costs, operating costs, and other system expenses have become critical in determining the profitability of HRESs. Given below are some of the most commonly used economic indexes.

7.1.1. Annual Global Cost (AGC). AGC is the sum of the system's capital, maintenance, and annual costs, as shown in equation (17).

$$\mathrm{AGC} = \mathrm{Ca}_{\mathrm{cap}} + \mathrm{Ca}_{\mathrm{main}}, \tag{17}$$

where $\mathrm{Ca}_{\mathrm{cap}}$ means the annual fundamental cost of the system and $\mathrm{Ca}_{\mathrm{main}}$ is the annual system maintenance cost.

7.1.2. Annualized Cost of the HRESs (ACHRES). The annualized cost of the HRESs (ACHRES) is the total of the annual replacement cost, annual capital cost, and annual maintenance cost of the HRESs given in equation (18).

$$\mathrm{ACHRES} = \mathrm{Ca}_{\mathrm{cap}} + \mathrm{Ca}_{\mathrm{main}} + \mathrm{Ca}_{\mathrm{rep}}, \tag{18}$$

where $\mathrm{Ca}_{\mathrm{rep}}$ means the annual replacement cost of the HRESs.

7.1.3. Cost of Energy (COE). The COE is calculated by dividing the annualized cost of the hybrid renewable energy system (ACHRES) by the total annual energy production (AOEP). It specifies the cost per unit of energy generated by HRESs given in equation (19).

$$COE = \frac{\sum_{i=1}^{n} \mathrm{ACHRES}}{\sum_{i=1}^{n} \mathrm{AOE}P_i}. \tag{19}$$

7.1.4. Life Cycle Cost (LCC). The net present value is calculated by adding the discounted capital, maintenance, and operating costs and subtracting the current revenues throughout the lifetime of the HRESs given in equation (20).

$$\mathrm{NPV} = \Sigma NPV_{\mathrm{end}} - C_{\mathrm{inv}} - \Sigma NPV_{OM} - \Sigma NPV_r, \tag{20}$$

where $\mathrm{NPV}_{\mathrm{end}}$ is the discounted income from the subsystems' residual value at the end of the HRESs' life; $C_{\mathrm{investment}}$ is the initial investment cost; $\mathrm{NPV}_{\mathrm{OM}}$ is the present value of future exploitation and maintenance costs, and NPV_r is the present value of future replacement costs to replace components during the system's life.

7.1.5. Levelized Cost of Energy (LCOE). LCOE is the sum of updated energy production costs divided by updated energy output (equation) (21).

$$\mathrm{LCOE} = \frac{\sum_{i=1}^{n} (1+r)^t}{\sum_{i=1}^{n} (1+r)^t}, \tag{21}$$

where n is the HRESs life, C_t is all costs, E_t is yearly clean energy output, and r is the annual discount rate.

7.1.6. Life Cycle Cost (LCC). Total HRES expenses (investment, operation, maintenance, replacement, etc.) − $\mathrm{S}_{\mathrm{NPV}}$ (net present value of revenue) given in equation (22)

$$\mathrm{LCC} = C + \mathrm{OM}_{\mathrm{NPV}} + R_{\mathrm{NPV}} - S_{\mathrm{NPV}}. \tag{22}$$

C = total HRES cost; $\mathrm{OM}_{\mathrm{NPV}}$ = maintenance and operation net present value; R_{NPV} = replacement net present value.

The detailed reliability indices of PV systems are presented for the selection and design of PV systems with system-level indexes, converter component indexes, load side indexes, and economic indexes.

8. Conclusion

In this paper, a 660 W PV system with a double boost converter is developed in MATLAB/Simulink and studied in three cases: constant solar irradiation, variable solar irradiation, and real-time irradiation data on May 2022. A PSO-based MPPT algorithm is implemented for extraction of maximum possible power from the PV source, and a detailed reliability index of a PV system is presented for analysis of the PV system at system-level indexes, converter component indexes, load side indexes, and economic indexes. The implemented converter will share the input current and reduce the current ripple and from analysis of the PV system in different input conditions, the system performance much relies on the solar irradiation availability, temperature, humidity, and geographical location of the plant.

Data Availability

The data used to support the findings of this study are available from the corresponding author upon request.

Conflicts of Interest

The authors declare that there are no conflicts of interest.

References

[1] A. Qazi, F. Hussain, N. Abd Rahim et al., "Towards sustainable energy: a systematic review of renewable energy sources, technologies, and public opinions," *IEEE Access*, vol. 7, pp. 63837–63851, 2019.

[2] R. Tiwari, K. Krishnamurthy, N. Ramesh Babu, P. Sanjeevi Kuma, and P. W. Wheeler, "Neural network based maximum power point tracking control with quadratic boost converter for PMSG-wind energy conversion system," *Electronics*, vol. 7, no. 20, pp. 1–17, 2018.

[3] B. P. Kumar, D. P. Winston, S. C. Christabel, and S. Venkatanarayanan, "Implementation of a switched PV technique for rooftop 2 kW solar PV to enhance power during unavoidable partial shading conditions," *Journal of Power Electronics*, vol. 17, no. 6, pp. 1600–1610, 2017.

[4] K. Kumar, N. Ramesh Babu, and K. R. Prabhu, "Design and analysis of RBFN-based single MPPT controller for hybrid solar and wind energy system," *IEEE Access*, vol. 5, pp. 15308–15317, 2017.

[5] A. M. Eltamaly, H. M. Farh, and M. F. Othman, "A novel evaluation index for the photovoltaic maximum power point tracker techniques," *Solar Energy*, vol. 174, pp. 940–956, 2018.

[6] K. Kumar, V. L. Devi, and M. D. Kumar, "Design of solar powered smart water pump for moisture controller in the agriculture sector," *Materials Today Proceedings*, 2022.

[7] D. P. Winston, B. P. Kumar, S. C. Christabel, A. J. Chamkha, and R. Sathyamurthy, "Maximum power extraction in solar renewable power system-a bypass diode scanning approach," *Computers & Electrical Engineering*, vol. 70, pp. 122–136, 2018.

[8] the-ministry, "The MNRE website," 2022, https://mnre.gov.in/the-ministry/physical-progress.

[9] D. Prince Winston, S. Kumaravel, B. Praveen Kumar, and S. Devakirubakaran, "Performance improvement of solar PV array topologies during various partial shading conditions," *Solar Energy*, vol. 196, pp. 228–242, 2020.

[10] K. Kumar, V. L. Devi, A. Prasad, H. R. Gali, and R. Tiwari, "Analysis of a fuel cell-fed BLDC motor drive with a double boost converter for electric vehicle application," in *Smart Grids for Renewable Energy Systems, Electric Vehicles and Energy Storage Systems*, pp. 59–75, CRC Press, Boca Raton, FL, USA, 2022.

[11] B. Aljafari, G. Devarajan, S. Arumugam, and I. Vairavasundaram, "Design and implementation of hybrid PV/Battery-Based improved single-endedprimary-inductorconverter-fed hybrid electric vehicle," *International Transactions on Electrical Energy Systems*, vol. 2022, p. 11, 2022.

[12] L. Atik, G. Bachir, and M. Aillerie, "Implementation of fuzzy logic MPPT in high-efficiency double boost DC-DC converter dedicated to photovoltaic sources," *Journal of Electrical Systems*, vol. 17, p. 3, 2021.

[13] K. Kumar, V. L. Devi, A. Prasad, R. Sarjila, and J. B. Edward, "Interpretation of PMSG-based wind system with high gain converters and MPPT controllers," in *Proceedings of the 2021 Innovations in Power and Advanced Computing Technologies (I-PACT)*, pp. 1–5, IEEE, Kuala Lumpur, Malaysia, November 2021.

[14] S. K. Mishra, S. K. Bhuyan, and P. V. Rathod, "Performance analysis of a hybrid renewable generation system connected to grid in the presence of DVR," *Ain Shams Engineering Journal*, vol. 13, no. 4, Article ID 101700, 2022.

[15] M. F. Guepfrih, G. Waltrich, T. B. Lazzarin, and B. Telles, "High step-up DC-DC converter using built-in transformer voltage multiplier cell and dual boost concepts," *IEEE Journal of Emerging and Selected Topics in Power Electronics*, vol. 9, no. 6, pp. 6700–6712, 2021.

[16] K. Kumar, R. Tiwari, N. R. Babu, and K. R. Prabhu, "Analysis of MISO super lift negative output Luo converter with MPPT for DC grid connected hybrid PV/wind system," *Energy Procedia*, vol. 145, pp. 345–350, 2018.

[17] S. N. Soheli, G. Sarowar, M. A. Hoque, and M. S. Hasan, "Design and analysis of a dc-dc buck-boost converter to achieve high efficiency and low voltage gain by using buck-boost topology into buck topology," in *Proceedings of the 2018 International Conference on Advancement in Electrical and Electronic Engineering (ICAEEE)*, pp. 1–4, IEEE, Gazipur, Bangladesh, November 2018.

[18] K. Kumar, N. R. Babu, and K. R. Prabhu, "Design and analysis of an integrated Cuk-SEPIC converter with MPPT for standalone wind/PV hybrid system," *International Journal of Renewable Energy Resources*, vol. 7, no. 1, pp. 96–106, 2017.

[19] J. Zhao, D. Chen, and J. Jiang, "Transformerless high step-up DC-DC converter with low voltage stress for fuel cells," *IEEE Access*, vol. 9, pp. 10228–10238, 2021.

[20] A. Amir, A. Amir, H. S. Che, A. Elkhateb, and N. A. Rahim, "Comparative analysis of high voltage gain DC-DC converter topologies for photovoltaic systems," *Renewable Energy*, vol. 136, pp. 1147–1163, 2019.

[21] O. Abutbul, A. Gherlitz, Y. Berkovich, and A. Ioinovici, "Stepup switching mode converter with high voltage gain using a switched-capacitor circuit," *IEEE Transactions on Circuits and Systems I: Fundamental Theory and Applications*, vol. 50, no. 8, pp. 1098–1102, 2003.

[22] B. Ju-Won, R. Myung-Hyo, K. Tae-Jin, Y. Dong-Wook, and K. Jong-Soo, "High boost converter using voltage multiplier," *Indust. Electronics Society, 31st Annual Conf. IEEE*, vol. 1, pp. 567–572, 2005.

[23] K. K. Law, K. W. E. Cheng, and Y. P. B. Yeung, "Design and analysis of switched-capacitor-based step-up resonant converters," *IEEE Transactions on Circuits and Systems I: Regular Papers*, vol. 52, no. 5, pp. 943–948, 2005.

[24] R. J. Wai and R. Y. Duan, "High step-up converter with coupled inductor," *IEEE Transactions on Power Electronics*, vol. 20, no. 5, pp. 1025–1035, 2005.

[25] R. J. Wai and R. Y. Duan, "High-efficiency DC/DC converter with high voltage gain," *IEE Proceedings - Electric Power Applications*, vol. 152, no. 4, pp. 793–802, 2005.

[26] K. Krishnamurthy, S. Padmanaban, F. Blaabjerg, R. B. Neelakandan, and K. R. Prabhu, "Power electronic converter configurations integration with hybrid energy sources–A comprehensive review for state-of-the-art in research," *Electric Power Components and Systems*, vol. 47, no. 18, pp. 1623–1650, 2019.

[27] M. A. Abdullah, T. Al-Hadhrami, C. W. Tan, and A. H. Yatim, "Towards green energy for smart cities: particle swarm optimization based MPPT approach," *IEEE Access*, vol. 6, pp. 58427–58438, 2018.

[28] A. P. Yoganandini and G. S. Anitha, "A modified particle swarm optimization algorithm to enhance MPPT in the PV array," *International Journal of Electrical and Computer Engineering*, vol. 10, no. 5, p. 5001, 2020.

[29] H. Li, D. Yang, W. Su, J. Lü, and X. Yu, "An overall distribution particle swarm optimization MPPT algorithm for photovoltaic system under partial shading," *IEEE Transactions on Industrial Electronics*, vol. 66, no. 1, pp. 265–275, 2019.

[30] Y. Kifle, B. Khan, and P. Singh, "Assessment and enhancement of distribution system reliability by renewable energy sources and energy storage," *Journal of Green Engineering*, vol. 8, no. 3, pp. 219–262, 2018.

[31] A. Sayed, M. El-Shimy, M. El-Metwally, and M. Elshahed, "Reliability, availability and maintainability analysis for grid-

connected solar photovoltaic systems," *Energies*, vol. 12, no. 7, p. 1213, 2019.

[32] E. Rakhshani, K. Rouzbehi, A. J Sánchez, A. C. Tobar, and E. Pouresmaeil, "Integration of large scale PV-based generation into power systems: a survey," *Energies*, vol. 12, no. 8, p. 1425, 2019.

[33] A. Sohani, M. H. Shahverdian, H. Sayyaadi et al., "Selecting the best nanofluid type for A photovoltaic thermal (PV/T) system based on reliability, efficiency, energy, economic, and environmental criteria," *Journal of the Taiwan Institute of Chemical Engineers*, vol. 124, pp. 351–358, 2021.

[34] P. Tu, S. Yang, and P. Wang, "Reliability-and cost-based redundancy design for the modular multilevel converter," *IEEE Transactions on Industrial Electronics*, vol. 66, no. 3, pp. 2333–2342, 2018.

[35] T. Dragičević, P. Wheeler, and F. Blaabjerg, "Artificial intelligence aided automated design for reliability of power electronic systems," *IEEE Transactions on Power Electronics*, vol. 34, no. 8, pp. 7161–7171, 2019.